Defect structure of yttria-stabilized zirconia and its influence on the ionic conductivity at elevated temperatures

J. P. Goff and W. Hayes

Oxford Physics, Clarendon Laboratory, Parks Road, Oxford, Oxfordshire, OX1 3PU, United Kingdom

S. Hull

ISIS Facility, Rutherford Appleton Laboratory, Chilton, Didcot, Oxfordshire, OX11 0QX, United Kingdom

M. T. Hutchings

National N.D.T. Centre, A.E.A. Technology Energy, E1 Culham, Abingdon, Oxfordshire, OX14 3DB, United Kingdom

K. N. Clausen

Condensed Matter Physics and Chemistry Department, Risø National Laboratory, DK-4000 Roskilde, Denmark

The defect structure of cubic fluorite structured yttria-stabilized zirconia $(ZrO_2)_{1-x}(Y_2O_3)_x$ has been investigated over the composition range $0.100(4) \leq x \leq 0.241(10)$ and temperatures $T(K)$ up to 2780(10) K, using single-crystal specimens. Analysis of neutron and x-ray diffraction data, including both Bragg and coherent diffuse scattering components, has identified three principal types of defects within the fluorite lattice. At low yttria concentrations ($x < \sim 0.15$) there are regions of the crystal ~ 20 Å in size which contain relatively few oxygen vacancies, causing the lattice to undergo a slight tetragonal distortion of the type observed in the tetragonal phase of $(ZrO_2)_{1-x}(Y_2O_3)_x$ at $x < \sim 0.09$. The oxygen vacancies are preferentially arranged in pairs on nearest-neighbor anion sites in the $\langle 111 \rangle$ fluorite directions, with a cation located between them and extensive relaxations of the surrounding nearest-neighbor cations and anions. As the yttria content increases, these $\langle 111 \rangle$ vacancy pairs pack together in $\langle 112 \rangle$ directions to form aggregates, whose short-range defect structure resembles the long-range crystal structure of the ordered compound $Zr_3Y_4O_{12}$ and other anion-deficient fluorite-related systems. The aggregates are typically ~ 15 Å in diameter, though both their size and number density increase slightly with x. On increasing the temperature, these aggregates remain stable up to close to the melting point. There is also an increasing number of single vacancies and $\langle 111 \rangle$ vacancy pairs (with surrounding relaxation fields) as x increases, and these isolated clusters become mobile at $T > \sim 1000$ K and give rise to the high ionic conductivity of the material. In light of these observations, we propose that the anomalous decrease in the ionic conductivity with increasing x is a consequence of the decreasing mobility of the isolated defects, possibly due to blockage by the increasing number of static aggregates. [S0163-1829(99)05621-0]

I. INTRODUCTION

A. Phase diagram and structure

Stabilized zirconia ceramics have been the subject of extensive scientific research owing to the diverse technological applications these materials find as fuel cells, oxygen sensors, and artificial diamonds.[1–3] Despite this attention, a number of questions remain to be resolved, including the temperature and concentration dependence of the structural disorder and its interrelationship with the high ionic conductivity which underlies many of the industrial uses of these systems. Zirconia-based ceramics can be formed by the addition of binary oxides such as CaO, MgO, La_2O_3, and Y_2O_3 to ZrO_2, but Y_2O_3 doping is particularly effective in producing high conductivities and is the most widely used.[1,2]

Pure zirconia, ZrO_2, adopts the monoclinic baddelyite structure [M-ZrO_2, space group $P2_1/c$ Ref. 4] under ambient conditions, with the Zr^{4+} in a distorted seven-fold coordination. On increasing the temperature, it transforms to a tetragonally distorted fluorite structure [T-ZrO_2, $P4_2/nmc$ (Ref. 5)] at $T \sim 1370$ K, with Zr^{4+} surrounded by eight an-

ions, but with two slightly different Zr^{4+}-O^{2-} distances. Perfect eightfold coordination is achieved at $T \sim 2643$ K with a transformation to a cubic fluorite structured phase [F-ZrO_2, $Fm\bar{3}m$ (Ref. 4)], followed by melting at $T \sim 2988$ K. The ambient temperature structure of yttria, Y_2O_3, has space group $1a\bar{3}$ and can also be derived from that of fluorite by removal of $\frac{1}{4}$ of the anions.[6] There are two six-fold-coordinated, symmetry-independent Y^{3+}, which have the anion vacancies arranged along either a face diagonal or a body diagonal. The only known ordered phase in the ZrO_2-Y_2O_3 system is $Zr_3Y_4O_{12}$. This adopts a rhombohedral structure which is also strongly related to that of fluorite,[7] though a more detailed description of the cation environment is deferred until Sec. V. It is important to note that the published phase diagram[8,9] represents the equilibrium states, derived from samples annealed for considerable times or prepared by coprecipitation methods. In practice, the cation mobility is sufficiently low that the high-temperature phases T and F can be retained for indefinite periods in the metastable state at ambient temperature. These so-called ''yttria-stabilized zir-

conias'' (YSZ) are labeled M^*, which is stable over the range $0 < x < {\sim}0.03$, T^* $({\sim}0.02 < x < {\sim}0.09)$, and F^* $({\sim}0.04 < x < {\sim}0.3)$.

B. Summary of previous literature

The published literature concerning the structural properties of stabilized zirconia ceramics is extensive, and only a brief summary is given here. It is now well documented that the effect of adding aliovalent cations such as Ca^{2+}, Mg^{2+}, La^{3+}, and Y^{3+} is to stabilize the high-temperature structures of ZrO_2 at room temperature (see Refs. 1 and 2, and references therein). The three metastable phases M^*, T^*, and F^* are analogous to the M, T, and F-phases, but with dopant cations located substitutionally on Zr^{4+} sites and a fraction of the oxygen sites vacant to retain overall electrical neutrality. These metastable phases have prolonged stability, and complete phase segregation requires prolonged annealing at temperatures below ${\sim}600$ K. It is also well known that neither the dopants nor the vacancies are randomly distributed throughout the M^*, T^*, and F^* lattices. Originally, electron diffraction investigations suggested that the metastable phases in $(ZrO_2)_{1-x}(CaO)_x$ contained coherent precipitates, typically ${\sim}30$ Å in size, of ordered phases such as Zr_4CaO_9.[10,11] However, numerous more recent x-ray and neutron diffraction studies have shown that the F^* phase in stabilized zirconia systems contains only locally ordered regions of vacancies and dopants.[12–31] The presence of these lattice defects causes extensive relaxations of the ions away from their regular fluorite lattice sites, though the nature of these displacements remains controversial. For example, Welberry et al.[24] were able to successfully account for the diffuse x-ray scattering measured from $(ZrO_2)_{1-x}(Y_2O_3)_x$ with $x = 0.20$ by allowing only the cations to move in $\langle 110 \rangle$ directions, with the extent of the relaxations dependent on their proximity to oxygen vacancies. Alternatively, single-crystal neutron diffraction studies of several $(ZrO_2)_{1-x}(Y_2O_3)_x$ systems by Argyriou et al.[27] showed the anions to be displaced predominantly in $\langle 001 \rangle$ directions from their lattice sites and, to a lesser extent, also in $\langle 111 \rangle$ directions. Other diffraction studies have also found evidence for anion relaxations along $\langle 001 \rangle$,[13,14] $\langle 111 \rangle$,[16,17] or both[12] and, in some cases, relaxations of cations along $\langle 111 \rangle$.[12–14] Similarly, there is conflicting evidence concerning the association between the dopant cations and the charge compensating anion vacancies, with reports that the O^{2-} vacancies are preferentially located near to either dopant[32–35] or host cations.[36–39]

Quasielastic light scattering studies showed that the high ionic conductivity σ of stabilized zirconia at elevated temperatures is due to the presence of highly mobile anion vacancies.[40] On increasing the temperature, σ rises more rapidly at temperatures above ${\sim}1000–1200$ K due to the breakup of vacancy clusters in the low-temperature ''associated regime'' and the onset of dynamic behavior of isolated vacancies.[41,42] However, this simple picture is not able to account for the dramatic variation of σ with dopant concentration (see Ref. 41 and references therein), where there is a maximum of σ at $x{\sim}0.08$ and a rapid decrease at higher concentrations. The explanation of this variation has provided a challenge to theoretical attempts

to model the microscopic diffusion mechanism within $(ZrO_2)_{1-x}(Y_2O_3)_x$.[35,39,43–52] Calculations using a simple model of a bound dopant-vacancy pair reproduce the peak in σ, but Hohnke[44] showed that the rapid decrease in σ with increasing x within the F^* phase can only be accounted for by including a free-energy-like function describing the ordering of vacancies by long-range defect interactions. Similarly, defect clusters formed by the aggregation of dopant cations to form deep traps which immobilize vacancies have been shown to give a qualitative agreement with the observed concentration dependence.[47] Furthermore, recent molecular dynamics simulations suggest that both the *number* and *size* of these clusters increases with increasing dopant content.[35]

From the above discussion it is clear that much of the published literature concerning the structural properties of stabilized zirconias is conflicting, due principally to the studies being performed on samples of different dopant species and concentration. To resolve some of these issues we have performed an extensive series of neutron and x-ray diffraction investigations over a wide range of dopant concentration for the $(ZrO_2)_{1-x}(Y_2O_3)_x$ system. Its principal aims are (i) to determine the structure of the defect clusters present within the cubic stabilized phase of $(ZrO_2)_{1-x}(Y_2O_3)_x$ and their structural relationships to ordered phases such as $Zr_3Y_4O_{12}$, (ii) to investigate the behavior of these clusters at elevated temperatures, and (iii) to combine the results of (i) and (ii) to explain the observed variation in the ionic conductivity σ with dopant concentration.

C. Outline of paper

In Sec. II we describe the theoretical aspects of the techniques used in this work, deriving the expressions used in the subsequent analysis of the experimental data. Neutron diffraction measurements have been employed to study both the Bragg and coherent diffuse scattering from single-crystal samples. X-ray diffuse scattering measurements are also presented. These complementary techniques exploit the particular sensitivity of the neutrons and x rays to the locations of the anions and cations, respectively. The use of these two techniques thus provides a stringent test of the proposed structural model. High-temperature studies of the quasielastic energy broadening of the neutron diffuse scattering are used to probe the dynamics of the defects at high temperatures. Details of the various experimental aspects of this work are presented in Sec. III, followed by a description of the experimental results in Sec. IV. While several neutron diffraction studies of stabilized zirconia ceramics have been presented in the literature recently (see, for example Refs. 18–22 and 25–28), in this work we present data collected over a much wider range of scattering vectors, for several yttria concentrations $[0.100(4) < x < 0.241(10)]$ and over a wide temperature range $[T(K) < 2780(10)$ K$]$. Section V contains a discussion of the structural model for $(ZrO_2)_{1-x}(Y_2O_3)_x$ derived in this work, including a comparison with other stabilized zirconia ceramics and ordered anion-deficient fluorite-related phases. The implications of the high-temperature results for the understanding of the high ionic conductivity of yttria-stabilized zirconia are also presented in Sec. V.

II. THEORY

The Van Hove coherent scattering function $S(\mathbf{Q},\omega)$ is related by double Fourier transform to the time-dependent total pair correlation function $G(\mathbf{r},t)$.[53] If one integrates $S(\mathbf{Q},\omega)$ over all energy transfers $\hbar\omega$ at constant $\mathbf{Q}$, one obtains the static structure factor $S(\mathbf{Q})$ which describes the instantaneous correlations between ions, in contrast to the elastic scattering which gives a time-averaged picture. In a neutron experiment, by making measurements away from Bragg points and by means of energy analysis, it is possible to separate the coherent diffuse component from the phonon scattering. Where the phonon scattering is small in comparison to the diffuse scattering, energy analysis is no longer required. Under these conditions diffuse x-ray scattering, which measures $S(\mathbf{Q})$, may also be used to study the disorder.

In practice, it is not possible to Fourier transform the diffuse scattering data for $S^D(\mathbf{Q},\omega)$ to yield $G^D(\mathbf{r},t)$. Instead, the data are usually interpreted in terms of a model of the disordered ions at assumed positions. The summation over ions may be converted to one over sites by defining the probability of occupation of each site in the crystal. For diffuse scattering we can calculate the coherent cross section from the occupation of sites relative to the ideal lattice. Thus a model for a cluster of defective ions of type i enables us to calculate the diffuse structure factor $F_i^D(\mathbf{Q})$ from

$$F_i^D(\mathbf{Q}) = \sum_j (p_j - c_j) a_j e^{-W_j(Q)} e^{-i\mathbf{Q}\cdot\mathbf{r}_j}, \qquad (1)$$

where the site j located at $\mathbf{r}_j$ is occupied with probability p_j (0 or 1) and c_j is unity when j coincides with a regular lattice site and zero elsewhere. a_j is the coherent scattering length for neutrons and the atomic form factor for x rays at the site j, and the Debye-Waller factor is given by $W_j = B_j Q^2/16\pi^2$, where B_j is the isotropic thermal vibration factor.

Depending on the relative values of a_j, the two types of scattering can thus be used to highlight different aspects of the disorder. Owing to the similarity in both scattering lengths and form factors, it is difficult to distinguish between the Zr^{4+} and Y^{3+} ions, and therefore we model the system in terms of an anion and "average" cation (subsequently labeled M). However, x-rays are more sensitive to the cations than the anions, while the scattering of neutrons from anions and cations is of similar magnitude.

If there is no correlation between the positions of the clusters, the scattering arising from each cluster is summed incoherently. All possible orientations and configurations of the clusters may be expected with equal probability, and the coherent scattering per defective ion is given by

$$S^D(\mathbf{Q}) = \frac{1}{N_i N_o} \sum_i^{N_o} |F_i^D(\mathbf{Q})|^2, \qquad (2)$$

where N_i is the number of defective anions in the cluster and N_o is the number of possible orientations of the cluster. At higher defect concentrations, the effects of correlations between clusters need to be taken into account, so that

$$S^D(\mathbf{Q}) = \frac{1}{N_i N_o N_c} \left[\sum_k e^{-i\mathbf{Q}\cdot\mathbf{R}_k} \right] \left[\sum_i |F_i^D(\mathbf{Q})|^2 \right], \qquad (3)$$

where there is a total of N_c clusters distributed over the sites k at the position vectors $\mathbf{R}_k$. It is assumed that an aggregate of clusters comprises only isolated defect clusters of the same type and orientation. If the clusters aggregate into small groups, with each cluster positioned at regular intervals in the lattice, one might expect to observe superlattice peaks, somewhat sharper in $\mathbf{Q}$ than the diffuse scattering from isolated clusters. The full width at half maximum Δ of the superlattice peak then enables a typical aggregate size $\xi \sim 1/\Delta$ to be estimated.

If the defects which give rise to the coherent diffuse intensity are static, then the neutron scattering will be elastic, i.e., $\omega = 0$. However, if, for example, the defects become mobile at an elevated temperature, there may be significant quasielastic energy broadening of the diffuse scattering. The spectral line shape of $S^D(\mathbf{Q},\omega)$ versus energy transfer ω then contains information on the temporal nature of the correlations between diffusing ions and the surrounding distorted lattice. In the simplest case, where the correlations decay exponentially with a lifetime τ_{coh}, the spatial and temporal behavior can be separated, such that

$$I^D(\mathbf{Q},t) = I^D(\mathbf{Q},0) e^{-t/\tau_{\text{coh}}}, \qquad (4)$$

giving a Lorentzian scattering function

$$S^D(\mathbf{Q},\omega) = \frac{S^D(\mathbf{Q})}{\pi\hbar} \frac{1/\tau_{\text{coh}}}{(1/\tau_{\text{coh}})^2 + \omega^2}. \qquad (5)$$

As a result, measurements of the quasielastic energy broadening of the coherent diffuse component can be used to study the dynamics of the defects which give rise to the scattering.

III. EXPERIMENTAL PROCEDURE

A. Sample preparation

The single-crystal samples of $(ZrO_2)_{1-x}(Y_2O_3)_x$ used in this work were grown in a cold crucible using direct radio frequency heating. Most of the crystals were provided by J. F. Wenckus of the Ceres Corporation, but the two samples with the highest dopant concentration [$x = 0.221(9)$ and $x = 0.241(10)$] were kindly loaned by J. D. Cummins of the University of Bath. The compositions determined using chemical analysis by A. G. Morton of UKAEA Harwell Laboratory are listed in Table I. For convenience, Table I includes both the yttria content x in $(ZrO_2)_{1-x}(Y_2O_3)_x$ and the total oxygen content z in $(Zr,Y)O_z$, where $z = (2+x)/(1+x)$. The samples were aligned and then cut ultrasonically into cylinders with the $[1\bar{1}0]$ crystallographic direction along the axis. In order to minimize the effects of extinction, relatively small 2-mm-diam samples were used for Bragg diffraction measurements. Larger, typically 15-mm-diam samples were used to study the much weaker quasielastic diffuse scattering. The samples for studies at elevated temperatures were encapsulated inside either molybdenum or tungsten cans, sealed under vacuum using electron beam welding techniques, and then mounted inside specially designed high-temperature furnaces, constructed of materials with low incoherent and absorption cross sections. The

TABLE I. Nominal yttria content of the $(ZrO_2)_{1-x}(Y_2O_3)_x$ samples used in this work, together with that measured by chemical analysis (x) and the total O^{2-} content (z). It is straightforward to show that $z = (2+x)/(1+x)$.

Nominal mol % Y_2O_3	Measured x in $(ZrO_2)/_{1-x}(Y_2O_3)_x$	Oxygen content z in $(Zr, Y)O_z$
9	0.100(4)	1.910(4)
12	0.126(5)	1.888(5)
15	0.158(6)	1.864(6)
18	0.184(7)	1.845(6)
21	0.221(9)	1.819(7)
24	0.241(10)	1.806(8)

sample chambers were heated under dynamic vacuum, and the temperatures were monitored and controlled using tungsten/rhenium thermocouples.

B. Neutrons

The defect structures of $(ZrO_2)_{1-x}(Y_2O_3)_x$ samples with $x=0.100(4)$ and $x=0.184(7)$ were investigated in detail at ambient temperature using the single-crystal diffractometer (SXD) at the ISIS Spallation Neutron Source.[54] This instrument is a time-of-flight Laue diffractometer which exploits the pulsed nature of the incident flux and uses a large area position-sensitive detector (PSD) to measure large volumes of reciprocal space at each crystal setting. The Bragg diffraction and diffuse scattering measurements were performed with the same experimental configuration. The PSD has an active area of $80\,mm \times 80\,mm$ with each pixel having $5\,mm \times 5\,mm$ spatial resolution. At its distance of 0.25 m, the detector subtends an angular range of some $20° \times 20°$ at the sample. All measurements were performed with the central pixel at $2\theta = 90°$ and in the horizontal scattering plane. The crystals were rotated in steps of $22.5°$, and the intensities of neutrons in the wavelength range $0.48\,Å \leq \lambda \leq 8.63\,Å$ were recorded using the time-of-flight technique. Adequate counting statistics for the Bragg diffraction and diffuse scattering measurements were collected after 2 and 10 h counting times, respectively.

A total of ~ 180 Bragg reflections were measured, out to a maximum $Q \sim 18.5\,Å^{-1}$. Intensities were extracted using standard procedures and normalized to remove the wavelength dependence of the incident neutron flux.[54] This process uses the intensity measured from a polycrystalline vanadium sample (which scatters neutrons incoherently) measured with the same experimental configuration. Following the application of wavelength-dependent extinction and reflectivity corrections, a total of ~ 70 independent Bragg intensities was obtained by averaging over equivalent reflections.

Preliminary investigations of the distribution of coherent elastic diffuse scattering indicated that the intensity lies predominantly in the $(1\bar{1}0)$ plane of reciprocal space, corresponding to scattering approximately in the horizontal plane of the detector. The time-of-flight spectra for the horizontal pixels were normalized using the same vanadium sample procedure discussed above. The normalized diffuse intensity was mapped onto the $(1\bar{1}0)$ plane of reciprocal space and

stored as a two-dimensional array with the x and y axes corresponding to the $[hh0]$ and $[00l]$ reciprocal space directions, respectively. The ranges covered by h and l were 0.0–8.0 and 0.0–10.0, respectively, both stored in steps of 0.1 reciprocal lattice units.

Studies of the quasielastic diffuse neutron scattering from crystals with a wide range of x were performed at ambient temperature and at elevated temperatures using triple-axis spectrometers at UKAEA Harwell Laboratory, Risø National Laboratory, and the Institut Laue-Langevin. If the coherent diffuse scattering is elastic or has quasielastic broadening well within the instrumental energy resolution (as is the case at room temperature), the intensity contours will be $S^D(\mathbf{Q})$. Neutrons of fixed incident energies $E_i = 14.4$ or 34.0 meV were selected using monochromator crystals, since they provide adequate coverage of the scattering plane and resolution for these measurements, and they allow higher-order contamination to be minimized using a pyrolitic graphite filter. Analyzer crystals were employed in order to reduce the background level and to discriminate against phonon scattering. The scattered elastic intensity was measured on a fine mesh of points in the $(1\bar{1}0)$ plane with increments in $\mathbf{Q}$ of 0.1 reciprocal lattice units. The high resolution required to investigate the energy broadening at elevated temperatures entails the use of ''cold'' moderated neutrons. A fixed incident energy of $E_i = 5.0$ meV was used, and in this case higher-order contamination was suppressed using a beryllium filter. Scans of energy transfer were performed at several fixed values of $\mathbf{Q}$ in the $(1\bar{1}0)$ plane in order to probe the dynamic nature of the disorder. The observed spectral line shapes could be fitted only by a combination of the Lorentzian function in Eq. (5) with the Gaussian instrumental energy resolution function, together with a linear background level. The elastic component contains contributions due to the incoherent scattering from the sample container and furnace.

In order to compare a snapshot of the dynamic disorder at elevated temperature with the static disorder at room temperature, it is necessary to measure $S^D(\mathbf{Q})$ over a comparable mesh in reciprocal space. However, it would be an extremely time-consuming procedure to measure the spectral line shape at each value of $\mathbf{Q}$ and then integrate over the energy transfer to give $S^D(\mathbf{Q})$. An attempt was made to approximate this by measuring the scattering intensity at a small, nonzero value of energy transfer of 0.50 meV. The intensity thus measured is related to $S^D(\mathbf{Q})$, but since it assumes that the energy width is independent of $\mathbf{Q}$, it provides only a qualitative measurement.

C. X rays

The x-ray measurements were performed at the Clarendon Laboratory, Oxford, using a Huber diffractometer and Cu $K\alpha$ radiation from a Stoe rotating anode source operating at 6 kW. In order to reduce the unwanted background, the instrument was used in the triple-axis configuration. Using flat pyrolytic graphite crystals for the monochromator and analyzer, the resolution in the scattering plane was approximately $0.01\,Å^{-1}$. The resolution perpendicular to this was determined by slits to be about $0.1\,Å^{-1}$.

The observed x-ray intensity $I^{\text{OBS}}(\mathbf{Q})$ may be related to the scattering function by

$$I^{\text{OBS}}(\mathbf{Q}) = CPAS(\mathbf{Q}) + D, \tag{6}$$

where C is a constant, P is the polarization correction, A is the absorption correction, and D is the "dark" background determined with the shutter closed. The radiation emerging from the rotating anode is assumed to be unpolarized, and P takes account of the partial polarization of the beam by the three reflecting crystals. Assuming that the crystals are ideally mosaic,

$$P = \frac{1 + \cos^2 \Phi_M \cos^2 \Phi_S \cos^2 \Phi_A}{1 + \cos^2 \Phi_M}, \tag{7}$$

where Φ_M, Φ_S, and Φ_A refer to the scattering angles of the monochromator, sample, and analyser, respectively. When x rays are scattered off a flat plate with negligible transmission, the absorption correction is given by

$$A^{-1} = \mu \left(1 + \frac{\sin \Psi}{\sin(\Phi_S - \Psi)} \right), \tag{8}$$

where μ is the linear absorption coefficient and Ψ is the angle between the incident beam and the plate.

The measurements are performed in reflection geometry because of the high absorption of x rays by the sample, and therefore access is limited to $0 \leq \Psi \leq \Phi_S$. Furthermore, Eq. (8) shows that the absorption correction is high over a large region close to $\Psi = \Phi_S$ and a smaller region near to $\Psi = 0$. This is a significant problem when trying to measure the already weak diffuse scattering. Thus, in order to achieve adequate coverage of the plane for comparison with the scattering function of Eq. (3) and the neutron scattering results, measurements must be performed with the surface normal in several crystallographic orientations.

For a cylindrical sample full access to the plane normal to the axis is available. A large cylinder was cut ultrasonically from the same single-crystal boule of $x = 0.184(7)$ material used for the neutron measurements, with $[1\bar{1}0]$ along the axis. The diameter was chosen to be large (12 mm) compared to the width of the beam (1 mm), so that provided Ψ was not too close to 0 or Φ_S, the flat plate absorption correction of Eq. (8) would be adequate. The large absorption corrections at low Q and the maximum scattering angle Φ_S attainable limit the measurements to the range $2.5 \leq Q \leq 6.0$ reciprocal lattice units.

IV. RESULTS

A. Neutron diffuse scattering survey

The coherent diffuse neutron scattering measured for all compositions in the $(1\bar{1}0)$ plane at room temperature is presented in Fig. 1. The scattering is found to be static within instrumental energy resolution [full width at half maximum (FWHM) $= 3.5$ meV]. The fact that the scattering is highly anisotropic rules out the possibility that the anion vacancies are distributed randomly over lattice sites with negligible

distortion fields. The contour plots in Fig. 1 show distinctive structural features which evolve with increasing vacancy concentration. For the $x = 0.100(4)$ sample, the most striking features are the broadened peaks centred at the "forbidden" (odd, odd, even) positions (112) and (114); see Fig. 1(a). As the dopant concentration is increased, these weaken [Figs. 1(a)–1(c)] so that for systems with $x > \sim 0.16$ their intensity is negligible [Figs. 1(d)–1(f)]. The diffuse features elsewhere become stronger and sharper with increasing yttria concentration. It is possible to index the strongest diffuse maxima with a superlattice displacement $\mathbf{q} = \pm(0.4, 0.4, \pm 0.8)$ from the regular Bragg reflections. However, some of the superlattice peaks are found to be much weaker than others so that they do not appear in the diffuse scattering intensity maps. This variation in intensity is determined by the defect structure factor $F_i^D(\mathbf{Q})$ [see Eq. (1)]. The out-of-plane diffuse elastic scattering intensity was measured for $(\text{ZrO}_2)_{1-x}(\text{Y}_2\text{O}_3)_x$ with $x = 0.126(5)$ using a triple-axis spectrometer with a tilting detector. This composition exhibits all of the features observed in the other samples [see Fig. 1(c)]. Only weak features are observed in the (100) plane, and these are found to be parts of the large peaks centered in the $(1\bar{1}0)$ plane. The diffuse scattering intensity is thus modulated in three dimensions in reciprocal space. However, the most intense features are centered in the $(1\bar{1}0)$ plane and we consider only this plane of reciprocal space in attempting to understand the origins of the coherent diffuse scattering. First, we establish the time-averaged structures of the sample with $x = 0.184(7)$.

B. Sample $(\text{ZrO}_2)_{1-x}(\text{Y}_2\text{O}_3)_x$ with $x = 0.184(7)$

1. Neutron Bragg scattering

Several sites within the fluorite lattice which may be occupied by cations and anions have been considered in the analysis of the Bragg scattering data. These are taken from previous work on anion deficient fluorite systems[12–17] and are illustrated in Fig. 2. A number of models for the average structure of $(\text{ZrO}_2)_{1-x}(\text{Y}_2\text{O}_3)_x$ have been derived (labeled I–V), based on different occupancies of the sites, and their reliability assessed by least-squares fitting to the experimental data for the squared structure factor F_{obs}^2. The principal criterion used in choosing appropriate models uses the weighted R-factor parameter R_w, given by

$$R_w^2 = \sum_{i=1}^{N} \frac{(F_{\text{obs}}^2 - F_{\text{calc}}^2)^2}{(\sigma F_{\text{obs}}^2)^2} \bigg/ \sum_{i=1}^{N} \frac{(F_{\text{obs}}^2)^2}{(\sigma F_{\text{obs}}^2)^2}. \tag{9}$$

The summations are made over the N measured reflections used in the fit. The expected R factor R_{exp} is given by

$$R_{\text{exp}}^2 = (N - P) \bigg/ \sum_{i=1}^{N} \frac{(F_{\text{obs}}^2)^2}{(\sigma F_{\text{obs}}^2)^2}, \tag{10}$$

where P is the number of fitted parameters. F_{calc}^2 is the square of the calculated Bragg structure factors, and σF_{obs}^2 is the estimated standard deviation on F_{obs}^2. The statistical significance of any improvements in R_w produced by the introduc-
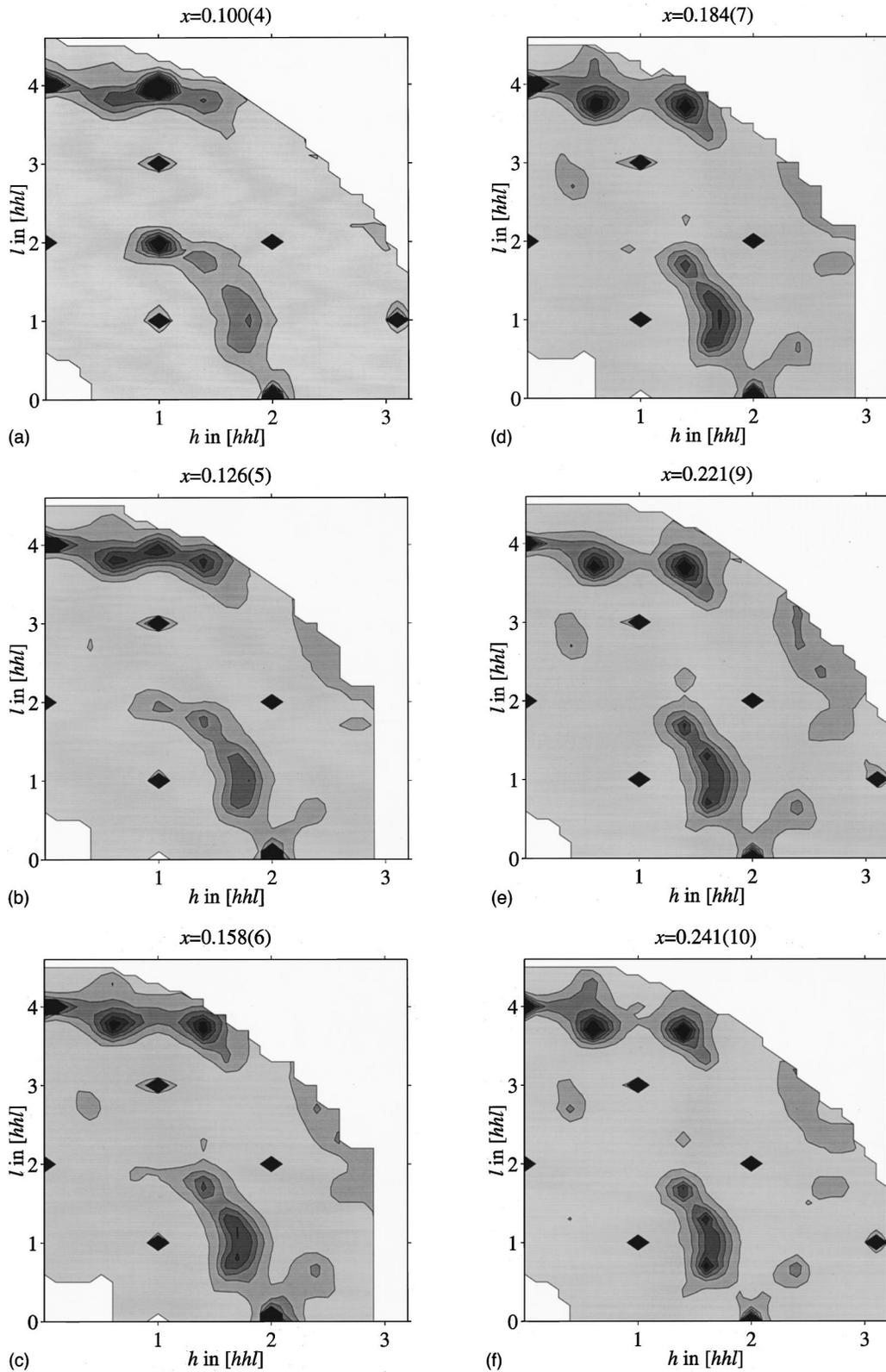
FIG. 1. Distribution of coherent diffuse elastic scattering $S^D(\mathbf{Q})$ in the $(1\bar{1}0)$ plane of reciprocal space at $T = 300$ K collected from samples with (a) $x = 0.100(4)$, (b) $x = 0.126(5)$, (c) $x = 0.158(6)$, (d) $x = 0.184(7)$, (e) $x = 0.221(9)$, and (f) $x = 0.241(10)$.

tion of additional fitted parameters has been assessed using the test proposed by Hamilton.[55] An additional constraint was placed on results of the fitting procedure requiring that the derived parameters have physically realistic values, principally with respect to the positional parameters (i.e., no anomalously short interionic distances) and the thermal vibration parameters $B_{(Zr,Y)}$ and B_O. The latter aspect has recently been addressed by Argyriou[25] who used powder neutron diffraction measurements of a $(ZrO_2)_{1-x}(Y_2O_3)_x$ sample with $x = 0.10$ as a function of temperature to separate
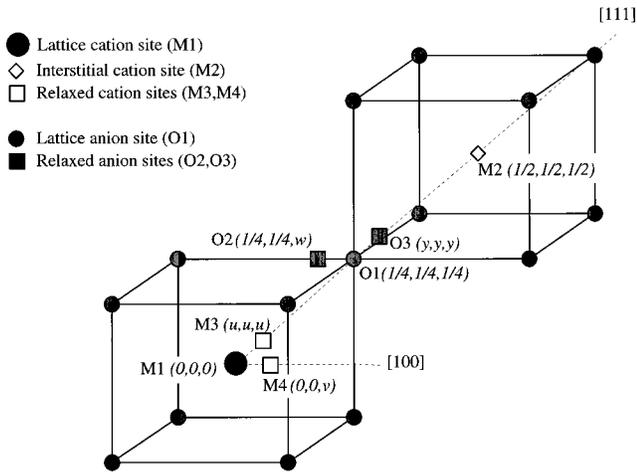
FIG. 2. Schematic diagram of a portion of the fluorite lattice illustrating the positions proposed to be occupied by anions and cations within F^* phases (Refs. 12–17) and used in the analysis of the Bragg diffraction data from $(ZrO_2)_{1-x}(Y_2O_3)_x$ samples with $x = 0.100(4)$ and $x = 0.184(7)$.

the contributions to the measured B values due to thermal vibration (B^{thermal}) and static disorder (B^{static}). At ambient temperature the true values of $B_{(Zr,Y)}^{\text{thermal}}$ and B_O^{thermal} are found to be ~ 0.3 and ~ 0.6 Å^2, respectively, close to the values observed in pure fluorite structured oxides and in the baddeleyite structured pure ZrO_2. As a consequence, any measured values for $B_{(Zr,Y)}$ and B_O significantly larger than these values suggest that the structural model used in the analysis does not completely describe the true disordered structure.

Model I is the simplest description of the average structure of $(ZrO_2)_{1-x}(Y_2O_3)_x$ and uses the perfect fluorite lattice with full occupancy of both anions in $4(a)$ sites at $(0,0,0)$, etc., and cations in $8(c)$ sites at $(\frac{1}{4},\frac{1}{4},\frac{1}{4})$, etc. The variable parameters in the fit are the scale factor S and the isotropic thermal vibration parameters $B_{(Zr,Y)}$ and B_O. As might be expected, this physically unrealistic model gives a relatively poor fit to the data, and in addition anomalously large values for both $B_{(Zr,Y)}$ and B_O (>1 Å^2) are obtained. The structural consequences of the addition of aliovalent Y^{3+} cations are introduced in model II, with charge compensation producing cation interstitials (IIa) or anion vacancies (IIb). In the former, extra cations are placed in the centers of the empty anion cubes in $4(b)$ sites at $(\frac{1}{2},\frac{1}{2},\frac{1}{2})$, etc., and an additional parameter (m_{M2}) allows the occupancy of the interstitial site to vary freely. This produces no significant improvement in the fit and a negligibly small value for m_{M2}. In contrast, a considerable reduction in R_w is observed with model IIb, where the occupancy of the lattice anion site O(1) ($m_{O(1)}$) is varied. However, the oxygen content obtained [$m_{O(1)} = 1.818(6)$] is somewhat lower than that expected on the basis of the known Y_2O_3 concentrations [$z = 1.845(6)$ for $x = 0.184(7)$; see Table I], suggesting additional relaxations of the surrounding anions away from the regular lattice sites. This possibility is considered in more detail in model III.

As discussed in Sec. I, previous studies of $(ZrO_2)_{1-x}(Y_2O_3)_x$ and $(ZrO_2)_{1-x}(CaO)_x$ using both neutron and x-ray diffraction have provided contradictory support for two additional O^{2-} sites which correspond to slight displacements of the lattice anions in the $\langle 001 \rangle$ and $\langle 111 \rangle$ directions.

In models IIIa and IIIb, we therefore introduce additional occupancy variables $m_{O(2)}$ and $m_{O(3)}$ corresponding to $48(g)$ sites at $(\frac{1}{4},\frac{1}{4},w)$, etc., with $w \sim 0.30$ and $32(f)$ sites at (y,y,y) with $y \sim 0.30$, respectively. At this stage we also impose the requirement of chemical neutrality by constraint of the total anion content to equal the value determined from the known Y_2O_3 content [i.e., $m_{O(1)} + m_{O(2)} + m_{O(3)} = z = (2+x)/(1+x)$]. Both models produce an improvement in R_w, though only in the case of model IIIa does the occupancy differ from zero by an amount outside its estimated standard deviation. Attempts to include both O(2) and O(3) sites simultaneously proved unstable due to excessive correlations between the occupancies, and we conclude that the only significant evidence is for slight anion displacements in $\langle 001 \rangle$ directions. All the fits discussed so far give excessively high values for $B_{(Zr,Y)}$ in the range 1–2 Å^2, and so in line with previous studies,[12–14] we now consider cation relaxations. These attempts (model IV) prove more conclusive than the anion case, with clear indications of displacements in $\langle 111 \rangle$ directions in model IVa which also reduces $B_{(Zr,Y)}$ significantly, to values ~ 0.5 Å^2. There is no evidence for $\langle 001 \rangle$ shifts in model IVb, which produces only minimal decrease in R_w and is somewhat unstable due to the essentially undetermined positional parameter ν.

The final model (V) for the disordered structure includes both the anion displacements in $\langle 001 \rangle$ and cation displacements in $\langle 111 \rangle$, derived from models IIIa and IVa, respectively. In common with models III and IV, model Va imposes the constraint that the thermal vibrations of the relaxed ions be equal to those of the lattice ions (i.e., $B_{M(3)} = B_{M(1)}$ and $B_{O(2)} = B_{O(1)}$). As shown in Table II, the simultaneous inclusion of displacements of both ionic species further reduces R_w, close to the expected value R_{exp}. Attempts to allow the relaxed and lattice ions to have different thermal vibration parameters in model Vb proved unsuccessful, with unstable minimisation of R_w due to excessive correlations between the variables. The final fitted parameters are listed in Table III.

2. Neutron diffuse scattering

The coherent diffuse neutron scattering intensity from the $(ZrO_2)_{1-x}(Y_2O_3)_x$ sample with $x = 0.184(7)$ in the $(1\bar{1}0)$ plane of reciprocal space is presented in Fig. 3(a). It is important to note that these data are measured on the SXD time-of-flight diffractometer,[54] which has the advantage of a large coverage of reciprocal space, but the disadvantage of no energy discrimination. However, the similarity between the data shown in Fig. 3(a) and those measured (over a smaller $\mathbf{Q}$ range) using the same sample on a triple-axis spectrometer with $\omega = 0$ confirms that the scattering is predominantly elastic in nature.

In regions of reciprocal space away from the regular fluorite Bragg reflections, two types of diffuse scattering are observed. First, there are regions of intensity which are rather broad in $\mathbf{Q}$, such as the scattering in the vicinity of $\mathbf{Q} \sim (1.7, 1.7, 1.0)$. These suggest the presence of rather small defect clusters. Second, there are somewhat narrower superlattice peaks displaced by $\mathbf{q} \sim \pm(0.4, 0.4, \pm 0.8)$ from the fluorite Bragg reflections. The width in $\mathbf{Q}$ of the superlattice peaks corresponds to a correlation length for the extended

TABLE II. Summary of the fits to the Bragg diffraction data from $(ZrO_2)_{1-x}(Y_2O_3)_x$ samples with $x = 0.100(4)$ and $x = 0.184(7)$ using the models I–V (see text). The weighted R factor R_w is defined in Eq. (9) and the expected R factor R_{exp} in Eq. (10).

Model	Description	R_w (%)	
		$x = 0.100(4)$	$x = 0.184(7)$
I	Regular fluorite	2.87	2.48
IIa	As model I, including cation interstitials	2.85	2.48
IIb	As model I, including anion vacancies	2.43	2.22
IIIa	As IIb but with anions relaxed in $\langle 001 \rangle$	2.29	2.02
IIIb	As IIb but with anions relaxed in $\langle 111 \rangle$	2.37	2.15
IVa	As IIb but with cations relaxed in $\langle 111 \rangle$	2.17	1.74
IVb	As IIb but with cations relaxed in $\langle 001 \rangle$	2.42	2.19
Va	Anions relaxed in $\langle 001 \rangle$ + cations in $\langle 111 \rangle$	2.01	1.44
Vb	As Va but independent thermal parameters	2.00	1.40
Expected R factor	R_{exp} (%)	1.79	1.21

defects of approximately 15 Å. There is not, therefore, segregation into microdomains of regular ordered phases, such as pure fluorite and/or $Zr_3Y_4O_{12}$. Instead, the superlattice peaks are ascribed to intercluster correlations from aggregates of smaller defect clusters arranged in a regular array.

In the regular fluorite structure, the anion sites are tetrahedrally coordinated by cations. When Zr^{4+} ions are substituted by aliovalent Y^{3+} ions, charge-compensating oxygen vacancies are required. Figures 4(a) and 4(b) depict two possible defect cluster models, comprising oxygen vacancies and their associated relaxation fields. The simplest defect cluster, based on an isolated oxygen vacancy, is shown in Fig. 4(a), and the divacancy defect cluster, which comprises a pair of oxygen vacancies separated by $(\frac{1}{2}, \frac{1}{2}, \frac{1}{2})$ across a cation, is shown in Fig. 4(b). It is assumed in each of these models that nearest-neighbor oxygen ions relax towards the vacancies along $\langle 001 \rangle$ directions and that nearest-neighbor cations relax away from the vacancies along $\langle 111 \rangle$ directions, following the results of the Bragg diffraction data discussed in the previous section. The divacancy defect clusters can be packed together separated by $(1, -\frac{1}{2}, \frac{1}{2})$ fluorite vectors in such a manner that the clusters fill space, and only the central cations and oxygen vacancy pairs are situated on regular fluorite sites. A small aggregate of divacancy clusters packed in this way will produce scattering displaced by $\mathbf{q} = \pm(0.4, 0.4, \pm 0.8)$ from all Bragg points, provided that the

enveloping structure factor from the individual divacancy cluster is large enough.

The calculated coherent diffuse neutron scattering intensity $S^D(\mathbf{Q})$ in the $(1\bar{1}0)$ plane using this defect model is presented in Fig. 3(b) for comparison with the experimental data in Fig. 3(a). The structure factor was calculated using Eqs. (1) and (3) for the divacancy model [Fig. 4(b)] with the positional parameters determined by neutron Bragg diffraction (Table III). Attempts to vary the positional parameters revealed that those obtained using neutron diffraction were close to the optimum values for the diffuse scattering. To reproduce the falloff in intensity with increasing $\mathbf{Q}$, the value of the anion thermal vibration parameter $B_{O(2)}$ used in the calculation of the diffuse scattering was slightly higher than that obtained from the Bragg diffraction data. This is probably a consequence of the greater sensitivity of the diffuse scattering to the displaced anions [O(2)], recalling that its thermal vibration parameter needed to be constrained to be equal to that of O(1) in the analysis presented in Sec. IV B 1. Superlattice peaks with the correct width in $\mathbf{Q}$ were obtained using Eq. (3) with an aggregate of divacancy clusters situated at $\mathbf{R}_k = (1, -\frac{1}{2}, \frac{1}{2})$, etc., within a radius of 10 Å and comprising some 15 clusters. The correlations within the aggregate which produce scattering at the regular fluorite Bragg positions are correlated with the host lattice over

TABLE III. Summary of the fitted parameters obtained from the analysis of the Bragg diffraction data from $(ZrO_2)_{1-x}(Y_2O_3)_x$ samples with $x = 0.100(4)$ and $x = 0.184(7)$ using model Va.

Parameter	Symbol	$x = 0.100(4)$	$x = 0.184(7)$
Scale factor	S	0.1522(7)	0.1717(6)
Cation thermal parameter	$B_{M(1)} = B_{M(3)}$ (Å^2)	0.24(5)	0.32(7)
Lattice cation occupancy	$m_{M(1)}$	0.71(8)	0.55(7)
Relaxed cation occupancy	$m_{M(3)}$	0.29(8)	0.45(7)
Relaxed cation position	u in (u,u,u)	0.028(2)	0.031(2)
Anion thermal parameter	$B_{O(1)} = B_{O(2)}$ (Å^2)	0.61(4)	0.55(3)
Lattice anion occupancy	$m_{O(1)}$	1.2(1)	0.8(1)
Relaxed anion occupancy	$m_{O(2)}$	0.7(1)	1.0(1)
Relaxed anion position	w in $(\frac{1}{4}, \frac{1}{4}, w)$	0.294(2)	0.291(2)
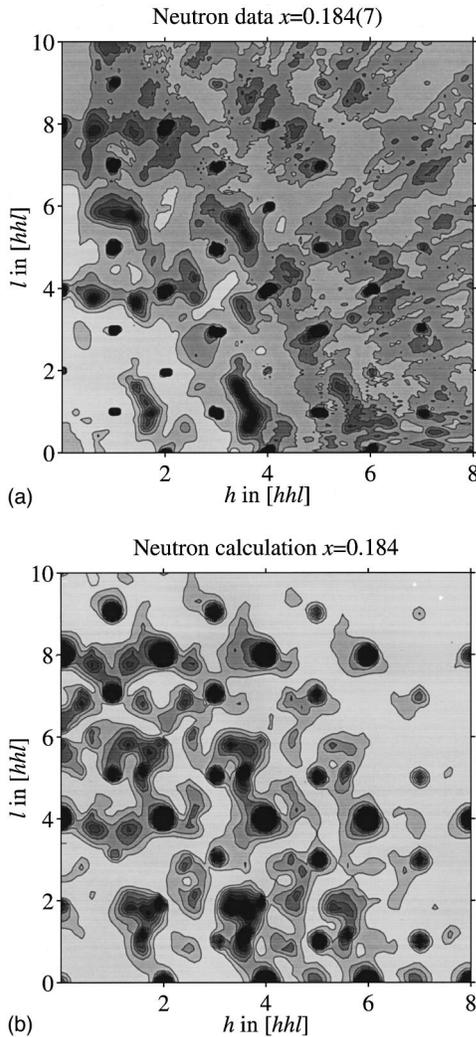
FIG. 3. (a) Distribution of coherent diffuse neutron elastic scattering $S^D(\mathbf{Q})$ in the $(1\bar{1}0)$ plane of reciprocal space at $T = 300\,\mathrm{K}$ collected from the sample with $x = 0.184(7)$ compared with (b) the calculated distribution of $S^D(\mathbf{Q})$ obtained using the model for the disordered structure described in the text.

FIG. 4. Schematic diagrams showing the defect structures of (a) an isolated single vacancy with associated relaxations of nearest-neighbor anions and cations, (b) a cation-centered vacancy pair in $\langle 111 \rangle$ with surrounding anion and cation relaxations, and (c) the tetragonal distortion of the fluorite cubic lattice due to alternate displacements of anions in $\langle 001 \rangle$ directions.

much longer range. Thus the broad features at the Bragg points in Fig. 3(b) arise as a consequence of the finite size of the aggregate and are in this case an artificial result of the calculation. In an attempt to reproduce some of the broader features in Fig. 3(a), particularly the intensity in the region $\mathbf{Q} \sim (1.7,1.7,1.0)$, the scattering from isolated divacancy clusters calculated using Eq. (2) was added incoherently. Unfortunately, the presence of the superlattice peaks at $\mathbf{Q} = (1.6,1.6,1.2)$ and $(1.6,1.6,0.8)$ makes it difficult to decide whether this scattering is associated with single-vacancy or divacancy clusters (Fig. 4). This question will be addressed further in Sec. IV D 1. Additional, more complex models for the aggregates were also considered, including the effects of a distribution of different aggregate sizes and asymmetric aggregates. However, none of these approaches gave significant improvements in the agreement between the calculation and measured data.

There are clearly some discrepancies between the calculation in Fig. 3(b) and the experiment in Fig. 3(a). One source of error in the calculation of the coherent diffuse scat-

tering is the assumption that all the ions within the defect clusters have exactly the same displacements. It is possible that a cluster in the center of an aggregate may have different relaxation fields than those closer to the edge of the aggregate or in isolated clusters. Furthermore, Zr^{4+} and Y^{3+} have different ionic radii, and the anion displacements are likely to depend upon the number and positions of neighboring dopant cations. These effects give rise to further static disorder which is difficult to model, and given the simplicity of the model, we conclude that the calculation agrees rather well with the experimental data.

3. X-ray diffuse scattering

The x-ray scattering intensity in the $(1\bar{1}0)$ plane measured from the $(ZrO_2)_{1-x}(Y_2O_3)_x$ sample with $x = 0.184(7)$ is shown in Fig. 5(a). The dark background [D in Eq. (6)] has been subtracted, but most of the remaining background was found to originate from the sample. Thus the whole of the remaining scattering has been corrected by the
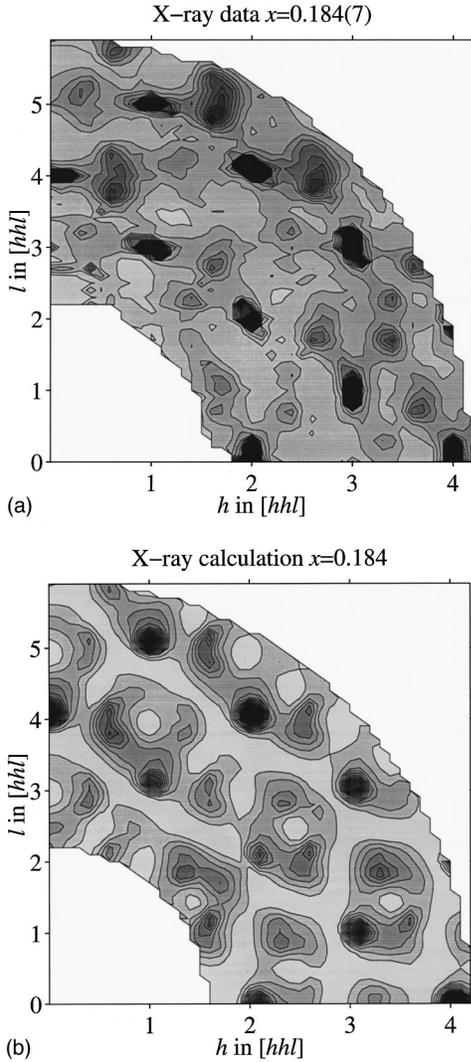
FIG. 5. (a) Distribution of coherent diffuse x-ray scattering $S^D(\mathbf{Q})$ in the $(1\bar{1}0)$ plane of reciprocal space at $T = 300$ K collected from the sample with $x = 0.184(7)$ compared with (b) the calculated distribution of $S^D(\mathbf{Q})$ obtained using the model for the disordered structure described in the text.

absorption and polarization factors in Eqs. (7) and (8). Measurements of the intensities of equivalent positions at $\mathbf{Q} = (h,h,\pm l)$ confirmed that the rather crude approximation in Eq. (8) is adequate to obtain a reliable qualitative picture of the distribution of diffuse scattering. The Bragg peaks are truncated in Fig. 5(a) in order to emphasize the diffuse scattering contours, and these are seen to differ markedly from the neutron data from the same composition in Fig. 3(a). Extra superlattice features are observed at $\mathbf{Q} \sim (0.4,0.4,5.2)$ and $(3.4,3.4,0.2)$ with x-rays, and the differences from the neutron results are particularly noticeable in the vicinity of $\mathbf{Q} \sim (1,1,4)$. The majority of the x-ray intensity in this region is concentrated at $\mathbf{Q} \sim (0.6,0.6,3.8)$ and $(0.6,0.6,4.2)$, whereas the neutron intensity is large for $\mathbf{Q} \sim (0.6,0.6,3.8)$ and $(1.4,1.4,3.8)$ and small for $\mathbf{Q} \sim (0.6,0.6,4.2)$.

The diffuse x-ray scattering intensity has been calculated using the appropriate form factors and the same defect model used for the diffuse neutron scattering described in Sec. IV B 2. The calculated contour pattern in the $(1\bar{1}0)$

plane is presented in Fig. 5(b). Once again, there are some minor discrepancies between the calculation and measured x-ray data [Fig. 5(a)], but overall the agreement is rather good. In particular, the x-ray structure factor successfully accounts for the changes in the intensity at $\mathbf{Q} \sim (0.6,0.6,4.2)$ and $(1.4,1.4,3.8)$ and the emergence of peaks near $\mathbf{Q} \sim (0.4,0.4,5.2)$ and $(3.4,3.4,0.2)$. This test using a complementary radiation confirms the defect model proposed in the previous section.

C. Sample $(\mathbf{ZrO_2})_{1-x}(\mathbf{Y_2O_3})_x$ with $x = 0.100(4)$

1. Neutron Bragg scattering

The Bragg scattering data from the $(ZrO_2)_{1-x}(Y_2O_3)_x$ sample with $x = 0.100(4)$ were analyzed using the same procedure employed for the $x = 0.184(7)$ composition (Sec. IV B 1), and lengthy details are not reproduced here. The values of R_w obtained in fits of models I–V are shown in Table II, and overall the conclusions are broadly the same as for the $x = 0.184(7)$ sample. There is evidence for the relaxation of anions in $\langle 001 \rangle$ and cations in $\langle 111 \rangle$ directions, with the final fitted parameters using model Va listed in Table III. The thermal vibration and positional parameters measured for the $x = 0.100(4)$ and $x = 0.184(7)$ samples agree within the estimated standard deviations, though the number of relaxed anions ($m_{O(2)}$) is somewhat lower in the former.

2. Neutron diffuse scattering

The coherent diffuse neutron scattering intensity measured in the $(1\bar{1}0)$ plane from the $(ZrO_2)_{1-x}(Y_2O_3)_x$ sample with $x = 0.100(4)$ is presented in Fig. 6(a). There are marked qualitative differences between these data and those obtained under identical conditions from the $x = 0.184(7)$ sample in Fig. 3(a). As remarked in Sec. IV A, strong peaks are observed at reciprocal lattice positions forbidden by the $Fm\bar{3}m$ symmetry of the fluorite structure. These extra peaks are observed for h odd and l even, but not for h even and l odd. The widths in $\mathbf{Q}$ are broader than those of the fluorite Bragg peaks and correspond to distorted regions of the lattice of size roughly 20 Å. The scattering at the superlattice positions is relatively weak, and the remaining scattering away from reciprocal lattice points is generally broad in $\mathbf{Q}$. This observation is, therefore, indicative of isolated defect clusters rather than the aggregates of clusters observed in $(ZrO_2)_{1-x}(Y_2O_3)_x$ with $x = 0.184(7)$.

The above ''forbidden'' reflections have also been observed in a previous neutron diffraction study of $(ZrO_2)_{1-x}(Y_2O_3)_x$ with $x = 0.09$.[15] These peaks were associated with a tetragonal distortion arising from small ordered displacements of the oxygen ions by δ in the $\langle 001 \rangle$ directions, as shown in Fig. 4(c). Such a model gives rise to scattering at the required (''forbidden'') reciprocal lattice points, with the optimum value $\delta = 0.044(1)$.[15] This value agrees well with that obtained by analysis of the regular Bragg scattering from our $x = 0.100(4)$ sample (see Table III).

In order to calculate the coherent diffuse scattering intensity from tetragonally distorted regions of the lattice, the anion defect cluster in Fig. 4(c) is used in Eq. (1), with the regular fluorite lattice vectors taken for $\mathbf{R}_k$ in Eq. (3). Aggre-
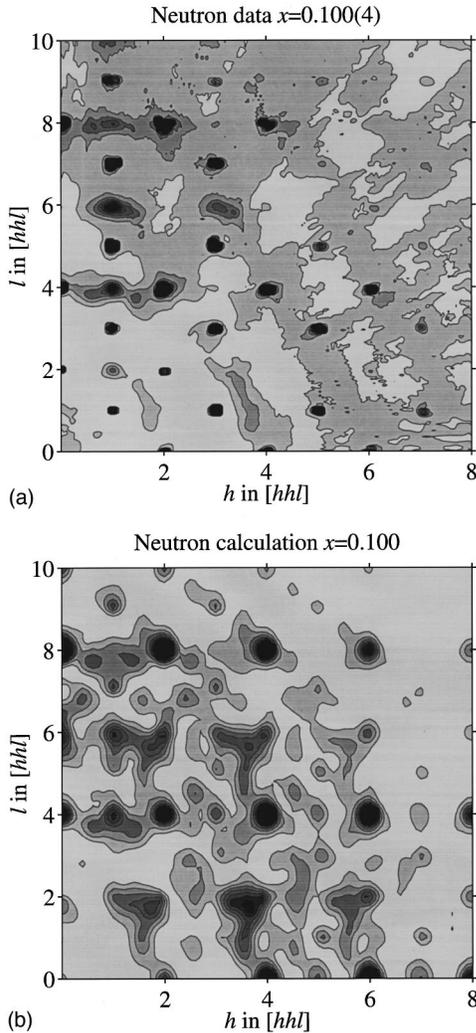
FIG. 6. (a) Distribution of coherent diffuse neutron elastic scattering $S^D(\mathbf{Q})$ in the $(1\bar{1}0)$ plane of reciprocal space at $T=300$ K collected from the sample with $x=0.100(4)$ compared with (b) the calculated distribution of $S^D(\mathbf{Q})$ obtained using the model for the disordered structure described in the text.

gates of these clusters with a width of roughly 20 Å reproduced the observed width in $\mathbf{Q}$ of the forbidden peaks. The scattering from the divacancy defect cluster model described in Sec. IV B 2 was also calculated and added incoherently. However, in this case the scattering was strongly weighted towards isolated defect clusters, and the relaxations used were those obtained in Sec. IV B 1 from the neutron diffraction results for $(\mathrm{ZrO_2})_{1-x}(\mathrm{Y_2O_3})_x$ with $x=0.184(7)$. The resultant calculated scattering intensity shown in Fig. 6(b) is, once again, in reasonably good agreement with the experimental data in Fig. 6(a).

D. Sample $(\mathrm{ZrO_2})_{1-x}(\mathrm{Y_2O_3})_x$ with $x=0.126(5)$

1. Neutron diffuse scattering

In the previous sections we have identified three types of defect present in yttria-stabilized cubic zirconia. These are (i) a localized tetragonal distortion of the cubic fluorite lattice in relatively vacancy free regions of the crystal, (ii) small defect clusters comprising a single vacancy or vacancy pair with

associated relaxations of the surrounding anions and cations, and (iii) aggregates of vacancy pair clusters with their surrounding relaxation fields packed together and separated by $(1,-\frac{1}{2},\frac{1}{2})$ lattice vectors. The relative concentration of each defect depends strongly on the yttria content x, but at least two types of defect coexist in any sample. By performing simulations of the diffuse scattering from each defect type in turn, it is possible to identify those regions of reciprocal space where the diffuse intensity is dominated by one type of defect. For the three defect types listed above, these positions are, respectively, (i) the integer (hkl) positions with h and k odd and l even, (ii) the region around $\mathbf{Q}=(1.7,1.7,1)$, and (iii) close to the most intense $\pm(0.4,0.4,\pm0.8)$ superlattice peaks which occur at $\mathbf{Q}=(1.4,1.4,1.8)$, $(1.6,1.6,0.8)$, and $(1.6,1.6,1.2)$. However, it should be emphasized that these scattering features are rather broad and there are relatively few positions in $\mathbf{Q}$ space where *all* the measured diffuse scattering arises from one defect type alone.

To investigate the interrelationship between the structural properties of $(\mathrm{ZrO_2})_{1-x}(\mathrm{Y_2O_3})_x$ and the behavior of its ionic conductivity, it is clearly necessary to perform experiments at elevated temperatures. Such measurements have been made using an $x=0.126(5)$ sample, since this composition contains measurable quantities of all three types of defect. Contour plots of the data collected at $T\sim293$, 1553, and 1803 K are illustrated in Figs. 7(a)–7(c), respectively, and show rather marked changes in the distribution of diffuse intensity. Overall, there is a reduction in the intensity due to the increase in the Debye-Waller factor, but in particular we note that the superlattice peaks at $\mathbf{Q}\sim(1.6,1.6,0.8)$ and $(\sim1.6,1.6,1.2)$ become more pronounced, while the broad region of scattering at $\mathbf{Q}\sim(1.7,1.7,1)$ disappears. However, it is important to note that the measured intensity is proportional to $\int_{-\varepsilon}^{+\varepsilon}S(\mathbf{Q},\omega)d\omega$ and the integration limits $\pm\varepsilon$ are determined by the instrumental resolution function in ω, which in this case is a Gaussian distribution of full width at half maximum 0.237 meV centered at $\omega=0.0$ meV. On a cautionary note, it must be stressed that the observed changes in the diffuse pattern could result from either changes in the defect structure and/or dynamic behavior of the defects causing quasielastic energy broadening of the diffuse scattering such that some intensity occurs at energy transfer values $\hbar\omega$ outside the measuring ''window'' determined by the Gaussian resolution function of the instrument. To resolve this question it is necessary to perform quasielastic scans of the energy transfer.

2. Quasielastic neutron scattering

The quasielastic scans were performed at eight different $\mathbf{Q}$ positions within the $(1\bar{1}0)$ plane. These were chosen to probe the dynamic nature of the three types of defect and avoid Bragg lines from the furnace components and spurious peaks due to higher-order contamination by $\lambda/2$ radiation. These $\mathbf{Q}$ positions are summarized in Table IV.

At room temperature the quasielastic scans at all $\mathbf{Q}$ positions were successfully fitted using a single Gaussian component of instrumental resolution width, indicating that all the defects are essentially static (i.e., $\tau>10^{-10}$ sec). However, at higher temperatures it proved necessary to include a second peak with a Lorentzian profile convolved with the
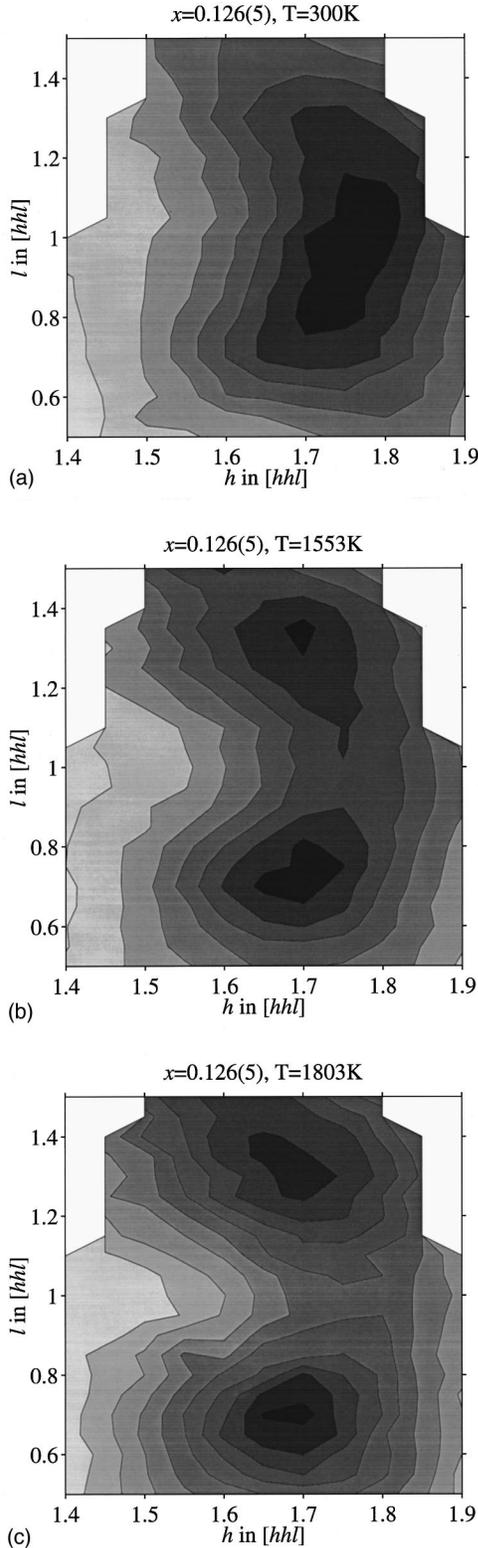
FIG. 7. (a) Distribution of coherent diffuse neutron elastic scattering $S^D(\mathbf{Q})$ in the $(1\bar{1}0)$ plane of reciprocal space collected from the sample with $x=0.126(5)$. Data are shown at (a) $T=300$ K, (b) $T=1553$ K, and (c) $T=1803$ K.

instrumental Gaussian function of the type discussed in Sec. II. Typical plots are shown in Fig. 8. It is clear that at $\mathbf{Q}=(1.05,1.05,1.95)$ and $(1.7,1.7,1.0)$ the Lorentzian component is significant at high temperature, whereas at

$\mathbf{Q}=(1.4,1.4,1.8)$ the diffuse scattering remains predominantly Gaussian in character. The results of the fitting of the quasielastic scattering data are given in Table V, which lists the Gaussian intensity at 293 K ($I_{G,293\,K}$), followed by its temperature dependence given as the scaled Gaussian ($I_G/I_{G,293\,K}$) and Lorentzian ($I_L/I_{G,293\,K}$) intensities and the Lorentzian width (FWHM$_L$) at the three temperatures studied. First, it is clear from Table V that the high-temperature behavior is significantly different for each of the three diffuse features listed in Table IV. This supports our earlier assumption that the diffuse scattering in the different regions of $\mathbf{Q}$ space arises from three different types of lattice defect. The Gaussian component of the quasielastic scattering due to the tetragonally distorted regions of the crystal decreases in intensity very rapidly, which we attribute to dynamic fluctuations between tetragonal and cubic symmetry. This may be caused by diffusion of isolated vacancies and/or vacancy pairs through the tetragonally distorted region, a fact confirmed by the significant Lorentzian component to the scattering arising from these defects. In contrast, it appears that the aggregates of vacancy pairs remain predominantly static up to the highest temperature measured. Indeed, subsequent measurements to $T=2780(10)$ K, albeit with slightly poorer resolution (FWHM$=0.90$ meV) confirmed that this statement remains true up to very close to the melting point. The implications of these observations for the conductivity mechanism in $(ZrO_2)_{1-x}(Y_2O_3)_x$ will be discussed in Sec. V B.

Having established that the diffuse scattering arising from the vacancy pair aggregates remains essentially elastic in nature, it is possible to separate the scattering contributions due to the aggregates and the smaller, dynamic units. By performing measurements at a fixed energy offset outside the elastic measuring "window," it is possible to estimate the $\mathbf{Q}$ variation of the scattering due to the mobile defects without this being masked by the intense superlattice peaks and, as a result, establish whether the mobile units are predominantly single vacancies or divacancies. Figure 9(a) shows the results of such a scan at $\hbar\omega=0.50$ meV. Figures 9(b) and 9(c) show the diffuse scattering calculated from an isolated single vacancy and a vacancy pair, respectively, including their associated inward relaxations of anions in $\langle 001 \rangle$ and outward relaxations of cations in $\langle 111 \rangle$. The displacements of the ions are taken to be the same as those derived in the room temperature model. While it is necessary to be cautious in interpreting measurements of this type, because they implicitly assume that the width of the Lorentzian component does not vary significantly with $\mathbf{Q}$, the good agreement between Figs. 9(a) and 9(c) provides strong evidence that the dominant mobile species at high temperatures is isolated anion vacancy pairs.

V. DISCUSSION

It is clear that the behavior of the Y^{3+}-doped system discussed above is rather different from the other widely studied case $(ZrO_2)_{1-x}(CaO)_x$. While the diffuse scattering due to the latter[21] is qualitatively similar to that observed here, it shows no variation with concentration over the range $0.04 \leqslant x \leqslant 0.20$,[21] does not change significantly on increasing temperature, and shows no evidence of quasielastic

TABLE IV. Summary of the **Q** positions in reciprocal space used for the high-temperature quasielastic neutron scattering investigations of the dynamics of the three types of disorder present in the $(ZrO_2)_{1-x}(Y_2O_3)_x$ sample with $x = 0.126(5)$.

Q	Diffuse feature	Defect type
(1.05,1.05,1.95)	Broad peak at ''forbidden'' (odd, odd, even) fluorite lattice position	Tetragonal distortion of the cubic lattice in relatively vacancy-free regions of the crystal
(1.75,1.75,1.0) (1.7,1.7,1.15)	Broad intensity between $Q = (1.6,1.6,0.8)$ and $\mathbf{Q} = (1.6,1.6,1.4)$ superlattice peaks	Isolated vacancy pairs with relaxations of surrounding anions and cations
(1,4,1.4,1.77) (1.3,1.3,1.7) (1.4,1.4,1.7) (1.6,1.6,1.3) (1.45,1.45,1.6)	Superlattice peaks located at $\mathbf{q} \pm (0.4,0.4,\pm 0.8)$ from the fluorite lattice positions	Aggregates of vacancy pairs and their associated relaxed surrounding ions.

broadening.[22] As might be expected, this suggests a profound difference in the conduction mechanism, and as a consequence, references to previously published work will be restricted to the $(ZrO_2)_{1-x}(Y_2O_3)_x$ system.

A. Defect clusters

Our observation of anion displacements in $\langle 001 \rangle$ directions and cation displacements in $\langle 111 \rangle$ directions is in agreement with some previous studies,[12–14,27] but in disagreement with others.[16,23] The differences probably result from difficulties in extracting reliable structural information from such compounds containing extensive lattice disorder. In particular, excessive correlations between the fitted thermal and static displacement parameters can occur during least-squares fitting, especially if only limited data sets are available. In support of our results, we recall that the measurements were performed up to high values of **Q** and the ionic displacements account satisfactorily for *both* the Bragg and diffuse scattering components. In the following subsections, we discuss the structural and dynamical properties of the $(ZrO_2)_{1-x}(Y_2O_3)_x$ system and the relationship between the defect cluster geometries and crystal structures of the phases present in the binary phase diagram.

1. Tetragonally distorted regions

The tetragonally distorted regions observed in this work are a representation of the ''internal deformation waves'' observed by Faber *et al.*[15] in an $x = 0.09$ sample as displacements of the anion sublattice in $\langle 001 \rangle$ directions. They can clearly be identified with the metastable tetragonal phase T^*-ZrO_2 which occurs at dopant levels less than $x \sim 0.09$ and the isostructural phase observed in pure ZrO_2 in the temperature range from ~ 1370 to ~ 2643 K. These tetragonal phases adopt space group $P4_2/nmc$ with lattice parameters a_{tet} and c_{tet} which correspond to $a_{fluorite}/\sqrt{2}$ and $a_{fluorite}$. In the conventional setting, with the inversion center at the origin, the (Zr,Y) are in $2(a)$ sites at $(\frac{3}{4},\frac{1}{4},\frac{3}{4})$ and $(\frac{1}{4},\frac{3}{4},\frac{3}{4})$ and the O in $4(d)$ sites at $(\frac{1}{4},\frac{1}{4},z_O)$, $(\frac{1}{4},\frac{1}{4},\frac{1}{2}+z_O)$, $(\frac{3}{4},\frac{3}{4},-z_O)$, and $(\frac{3}{4},\frac{3}{4},\frac{1}{2}-z_O)$. The displacement of the anions from their ''ideal'' fluorite positions at $z_O = \frac{1}{2}$ is then equivalent to the displacement of the anions in $\langle 001 \rangle$ directions, w, in Sec. IV A. However, direct comparison of the values using the Bragg results presented in Table III for our $x = 0.100(4)$

sample are difficult because the value of w includes a contribution from the relaxed anions surrounding the vacancy clusters and the most relevant value is that used to calculate the diffuse scattering, $w = 0.044$. In the high-temperature pure material, a value of 0.065 has been reported,[5] while for a mixed-phase ($T^* + F^*$) sample with $x = 0.03$ the value is $0.0436(1)$.[26]

Recent convergent beam electron diffraction studies of ZrO_2-9.9 mol % Y_2O_3 samples proposed that the presence of additional reflections at ''forbidden'' (odd, odd, even) fluorite positions such as $\mathbf{Q} = (1,1,2)$ and $(1,1,4)$ results from collective displacements of the anions in $\langle 111 \rangle$ rather than $\langle 001 \rangle$ directions.[56] The cubic symmetry is retained, but the loss of the face center symmetry operation leads to space group $P\bar{4}3m$. However, for space group $P\bar{4}3m$, all (hkl)
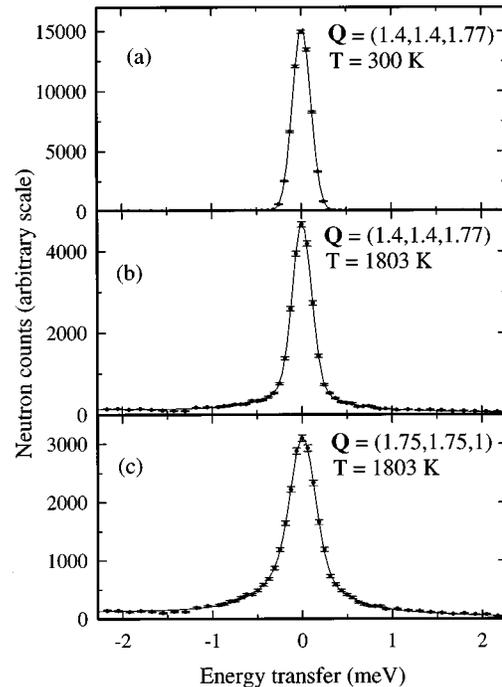
FIG. 8. Energy scans at constant **Q** through the quasielastic diffuse scattering from the $x = 0.126(5)$ sample. The experimental data are fitted by a combination of a resolution-limited Gaussian peak, a broadened Lorentzian component convolved with the Gaussian resolution function, and a linear background contribution.

TABLE V. Temperature variation of the intensity of the Gaussian (I_G) and Lorentzian (I_L) components of the quasielastic energy scans and the width of the Lorentzian component (FWHM$_L$) at $T = 293$, 1173, 1553, and 1803 K.

Q	293 K $I_{G,293\,K}$	1173 K $I_G/I_{G,293\,K}$	$I_L/I_{G,293\,K}$	FWHM$_L$ (meV)	1553 K $I_G/I_{G,293\,K}$	$I_L/I_{G,293\,K}$	FWHM$_L$ (meV)	1803 K $I_G/I_{G,293\,K}$	$I_L/I_{G,293\,K}$	FWHM$_L$ (meV)
(1.05,1.05,1.95)	1223(8)	0.361(4)	0.144(6)	0.62(4)	0.106(7)	0.233(6)	0.70(1)	0.049(9)	0.256(8)	0.99(1)
(1.75,1.75,1.0)	2393(7)	0.605(3)	0.109(5)	0.31(2)	0.210(4)	0.269(6)	0.44(3)	0.1071(8)	0.305(8)	0.46(2)
(1.7,1.7,1.15)	2199(9)	0.619(4)	0.103(5)	0.38(2)	0.272(5)	0.220(7)	0.52(4)	0.131(7)	0.256(8)	0.56(3)
(1.4,1.4,1.77)	1873(9)	0.758(4)	0.098(6)	0.45(4)	0.424(5)	0.163(5)	0.48(3)	0.258(8)	0.201(6)	0.66(4)
(1.3,1.3,1.7)	1202(7)	0.701(4)	0.121(5)	0.62(5)	0.405(6)	0.213(6)	0.50(4)	0.275(8)	0.225(7)	0.74(4)
(1.4,1.4,1.7)	1759(6)	0.812(5)	0.092(5)	0.44(4)	0.454(6)	0.151(6)	0.48(3)	0.301(9)	0.177(7)	0.67(4)
(1.6,1.6,1.3)	1733(6)	0.797(4)	0.086(5)	0.54(7)	0.445(5)	0.142(7)	0.62(4)	0.289(8)	0.167(6)	0.74(4)
(1.45,1.45,1.6)	1395(6)	0.807(5)	0.087(6)	0.45(4)	0.514(6)	0.136(6)	0.60(4)	0.358(8)	0.168(7)	0.62(3)

reflections are allowed and calculations of the diffuse scattering from the proposed defect cluster generate a number of broad peaks with significant intensity at positions such as $Q \sim (5,5,0)$. With reference to Fig. 6(a), no peak is observed at this position and our neutron diffraction studies do not support this structural model.

2. Divacancy pairs

The second type of defect cluster discussed previously is the cation-centered vacancy pair along a $\langle 111 \rangle$ fluorite direction, with its associated relaxations of the surrounding anions and cations. It is now widely accepted that these $\langle 111 \rangle$ vacancy pairs are a general structural motif in ordered anion-deficient fluorite related superstructures.[7,57–64] The inclusion of these vacancy pairs and their surrounding relaxation field replaces an M_7O_{14} fragment of the fluorite lattice with $M(1)_1M(2)_6O(2)_{12}V_2$, where $M(1)$ is the central cation, $M(2)$ are the relaxed nearest-neighbor cations, O(2) are the relaxed nearest-neighbor anions and V denotes an anion vacancy. This process makes one of the cubic threefold axes unique, and as might then be expected, many of the ordered phases adopt rhombohedral space groups such as $R3$ and $R\bar{3}$. At stoichiometries close to MO_2, these units are isolated [i.e., γ-$Zr_5Sc_2O_{13}$ (Ref. 60)], but increased numbers of vacancies are accommodated by the formation of infinite strings of vacancy pairs in compounds such as δ-$Zr_3Sc_4O_{12}$,[60] Φ-$Ca_2Hf_7O_{16}$,[62] Φ_1-$CaZr_4O_9$,[64] and Φ_2-$Ca_6Hf_{14}O_{44}$.[63] Indeed, the C-type structure of the end member Y_2O_3 can be considered as an interwoven array of $\langle 111 \rangle$ vacancy pair strings,[6] leading to two different cation environments in space group $Ia\bar{3}$. A comprehensive study of fluorite related anion-deficient compounds using powder x-ray diffraction techniques has been reported,[61] and the nearest-neighbor anions are found to relax towards the vacancies by ~ 0.3 Å in approximately the $\langle 100 \rangle$ directions and the nearest-neighbor cations relax away by ~ 0.2 Å in close to $\langle 111 \rangle$ directions of the fluorite supercell. The extent of these relaxations and their general directions are, therefore, close to the distances found in this work.

3. Vacancy pair aggregates

The final type of defect to be considered is the aggregate clusters formed by packing the $M_7O_{12}V_2$ structural motifs in $\langle 112 \rangle$ directions. This process leads to the closest possible packing of these units, giving overall M_7O_{12} stoichiometry. As a result, the most relevant ordered phase to consider is $Zr_3Y_4O_{12}$. This compound has been shown to adopt the rhombohedral δ phase [first identified in the $(ZrO_2)_{1-x}(Sc_2O_3)_x$ system (Ref. 60)] with space group $R\bar{3}$. As illustrated in Fig. 10, the structure of $Zr_3Y_4O_{12}$ is derived from that of fluorite.[7,58] The ordering of the vacancy pairs leads to two different cation sites, one sixfold and one sevenfold coordinated. These can be equated to the $M(1)$ and $M(2)$ cation positions found in the defect clusters (Fig. 2). The hexagonal cell constants are related to those of fluorite by $a_{hex} = \sqrt{\frac{7}{3}} a_{fluorite}$ and $c_{hex} = \sqrt{3} a_{fluorite}$ and the positional parameters by

$$\begin{pmatrix} x_{hex} \\ y_{hex} \\ z_{hex} \end{pmatrix} = \begin{pmatrix} \frac{1}{2} & 1 & -\frac{3}{2} \\ -\frac{3}{2} & \frac{1}{2} & 1 \\ 1 & 1 & 1 \end{pmatrix} \begin{pmatrix} x_{fluorite} \\ y_{fluorite} \\ z_{fluorite} \end{pmatrix}.$$

We may, therefore, transpose the positions of the anions and cations within the defects into this hexagonal setting and compare these with the corresponding positions in the $Zr_3Y_4O_{12}$ structure using the values obtained by x-ray techniques.[7] As shown in Table VI, these values are in good accord, supporting our suggestion of a strong structural relationship between the defect cluster aggregates and the long-range-ordered compound.

So far, the discussion has not addressed the question of Zr^{4+}/Y^{3+} cation ordering and whether these two species are randomly distributed over the $M(1)$ and $M(2)$ sites. Experimentally, in this work and the previous x-ray and neutron studies,[12–16] it has not proved possible to distinguish between the host and dopant cations due to the relative similarity of the scattering powers for Zr^{4+} and Y^{3+} for both types of radiation. In principle, extended x-ray absorption fine structure (EXAFS) spectroscopy is a powerful technique to probe the individual coordination polyhedra surrounding each cation species, but the published studies to date are contradictory, with opposing evidence for the vacancies being preferentially associated with the host[32–34] and dopant[36–38] cations. Intuitively, one might expect the central cation [$M(1)$] to be Y^{3+}, since this corresponds to one of the cation environments observed in pure Y_2O_3.[6] However, an extensive study of M_7O_{12}-type phases[61] indicated that, in those cases where cation ordering is observed, it is the smaller (more highly

x=0.126(5), T=1803K, Energy=0.5meV

(a)

Calculation: single vacancy cluster

(b)

Calculation: isolated divacancy cluster

(c)
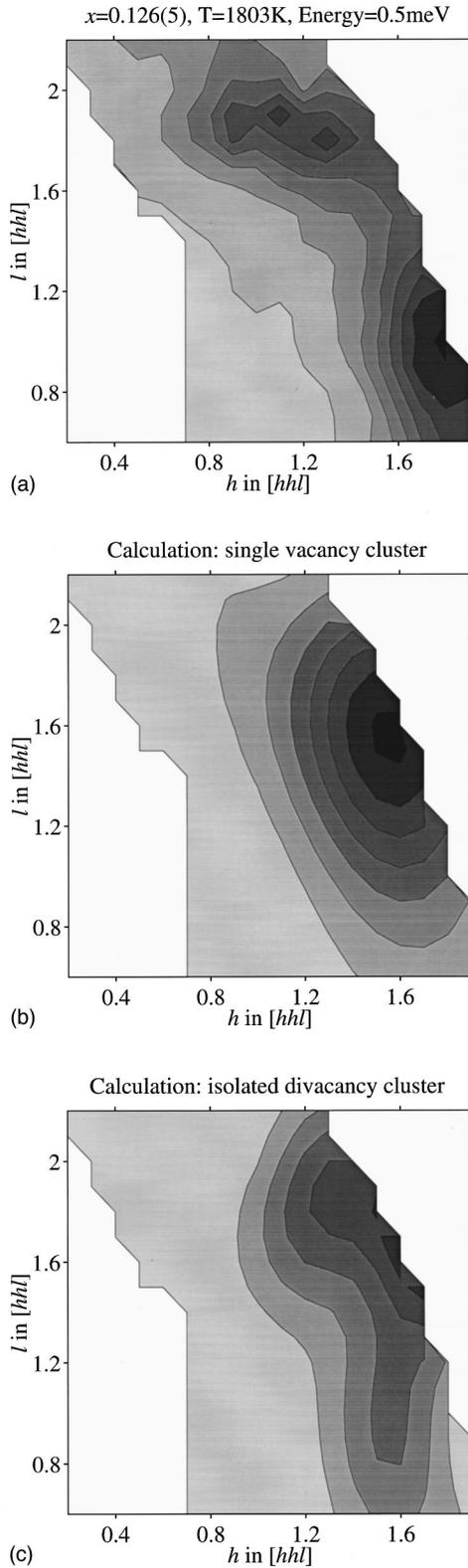
FIG. 9. (a) Distribution of coherent diffuse neutron scattering $S^D(\mathbf{Q},\omega)$ in the $(1\bar{1}0)$ plane of reciprocal space collected from the sample with $x=0.126(5)$ at $T=1803$ K with a fixed energy transfer $\hbar\omega=0.50$ meV. This is compared with (b) the calculated distribution of $S^D(\mathbf{Q})$ for an isolated single vacancy and (c) an isolated divacancy pair, both with surrounding relaxations of the surrounding anions and cations as illustrated in Figs. 4(a) and 4(b), respectively.
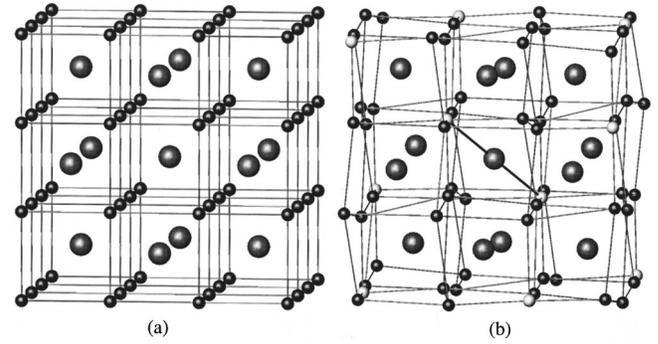
FIG. 10. Schematic diagram of the structure of (a) fluorite structured pure ZrO_2 and (b) the ordered compound $Zr_3Y_4O_{12}$ (Ref. 7) illustrating their structural similarity. The larger dark spheres are Zr^{4+}/Y^{3+} and the smaller dark spheres are O^{2-}. The lighter spheres in (b) represent anions sites that are empty in $Zr_3Y_4O_{12}$.

charged) species that adopts sixfold coordination. For example, taking the anion displacement parameter $w=0.041$ (Table III) and the ionic radius of O^{2-} to be 1.40 Å,[65] the cavity around the $M(1)$ site can accommodate a cation of maximum radius 0.75 Å. The relative sizes of Zr^{4+} ($r=0.82$ Å) and Y^{3+} ($r=0.96$ Å) (Ref. 65) suggests that the former is more likely to be situated on $M(1)$ sites, with local charge neutrality maintained by filling the $M(2)$ sites with both Zr^{4+} and Y^{3+} in the ratio 1:2. Further support for this assignment is provided by the x-ray diffraction studies of the system $Zr_3Yb_4O_{12}$,[57] because the ionic radii of Y^{3+} ($r=0.96$ Å) and Yb^{3+} ($r=0.93$ Å) (Ref. 65) are relatively similar, but the scattering contrast between host and dopant cation is increased. The cations are randomly distributed over the $M(1)$ and $M(2)$ sites at high temperature, but on

TABLE VI. Comparison of the lattice coordinates of the various ionic species within the divacancy cluster aggregate, the M_7O_{12} fragment observed in the ordered compound $Zr_3Y_4O_{12}$ (Ref. 7), and the ideal fluorite lattice.

Ion		Divacancy aggregate	M_7O_{12} fragment	Fluorite lattice
Central cation $[M(1)]$	x	0	0	0
	y	0	0	0
	z	0	0	0
Anion vacancy (V)	x	$\frac{1}{4}$	$\frac{1}{4}$	$\frac{1}{4}$
	y	$\frac{1}{4}$	$\frac{1}{4}$	$\frac{1}{4}$
	z	$\frac{1}{4}$	$\frac{1}{4}$	$\frac{1}{4}$
Relaxed cation $[M(2)]$	x	0.544	0.522	$\frac{1}{2}$
	y	0.544	0.531	$\frac{1}{2}$
	z	-0.044	-0.010	0
Relaxed anion $[O(2)]$	x	$\frac{1}{4}$	0.226	$\frac{1}{4}$
	y	$\frac{1}{4}$	0.255	$\frac{1}{4}$
	z	0.710	0.7148	$\frac{3}{4}$
Relaxed anion $[O(2')]$	x	$\frac{1}{4}$	0.244	$\frac{1}{4}$
	y	$\frac{1}{4}$	0.252	$\frac{1}{4}$
	z	-0.210	-0.189	$-\frac{1}{4}$

FIG. 11. Variation of (a) the approximate size of the divacancy aggregate clusters, (b) the intensity of the diffuse superlattice peak at $\mathbf{Q}=(0.6,0.6,3.8)$, and (c) the intensity of the diffuse scattering at $\mathbf{Q}=(1.7,1.7,1.0)$ with yttria content x in $(ZrO_2)_{1-x}(Y_2O_3)_x$.

cooling Zr^{4+} become concentrated on the $M(1)$ site with little or no occupancy by Yb^{3+}.[57]

It is of interest to note that the structural similarities between the defects and ordered compounds observed in the anion-deficient fluorite compound $(ZrO_2)_{1-x}(Y_2O_3)_x$ are mirrored by the anion-excess fluorites. For example, the defects observed in $(CaF_2)_{1-x}(YF_3)_x$ can be described as fragments of the structure of $Ca_{14}Y_5F_{43}$.[66] Clearly, detailed structural studies of anion-deficient and anion-excess systems are required to establish whether this is a general feature of fluorite related compounds.

4. Size of aggregates

We now return to the diffuse scattering data collected over a range of concentrations [Figs. 1(a)–1(e)] and consider the variation of the defect properties with yttria content x in more detail. The diffuse neutron scattering intensity has been placed on an absolute scale by reference to the observed intensities of phonon excitations, and scans of wave-vector transfer in the $[hh0]$ direction through the superlattice scattering at $\mathbf{Q}=(0.6,0.6,3.8)$ have been fitted to Lorentzian profiles. The widths of these peaks are related to the size of the divacancy aggregates (see Sec. II), and the correlation lengths ξ are plotted as a function of Y_2O_3 concentration x in Fig. 11(a). At the lowest concentration the size is comparable to that of an isolated divacancy cluster. However, the correlation length is found to increase in proportion to the dopant concentration. This shows that the vacancy pair aggregates increase in size, in agreement with the predictions of recent molecular dynamics simulations.[35] In addition, the intensities of the superlattice peaks depend upon the number of divacancy clusters incorporated in aggregates. The integrated in-

tensities at $\mathbf{Q}=(0.6,0.6,3.8)$ shown in Fig. 11(b) increase with dopant concentration, showing that more clusters are present in the aggregates. However, the increase in intensity with x is considerably smaller than would be expected if all the extra charge-compensating vacancies were part of large aggregates. Figure 11(c) shows the intensity at $\mathbf{Q}=(1.7,1.7,1)$ as a function of composition. This broad scattering arises primarily from smaller defect clusters, and the fact that this increases with dopant concentration demonstrates that the number of isolated defect clusters also increases.

B. Dynamics

The composition dependence of the ionic conductivity of yttria-stabilized zirconia may be understood in terms of the model of the disorder developed above. For dopant concentrations $x < \sim 0.10$, the charge-compensating vacancies are accommodated in isolated divacancy clusters. The quasielastic energy broadening of the diffuse neutron scattering at elevated temperature demonstrates that these defects become mobile and are able to contribute to the superionic conductivity. In this regime the increasing dopant concentration produces a larger number of charge carriers and the conductivity rises. However, above this concentration the number of defect clusters increases to balance the charge of the Y^{3+} ions, but we have shown that some of these clusters are incorporated into larger vacancy pair aggregates. The diffuse neutron scattering at the superlattice positions does not broaden in energy transfer at high temperature, showing that this disorder is static and vacancies trapped within the aggregates do not contribute significantly to the ionic conductivity. In simple terms, the bulk ionic conductivity may be suppressed by two mechanisms. First, an increasing number of O^{2-} vacancies are trapped inside the large aggregates, and this reduces the number of mobile species. Second, the aggregate regions are increasing in size, which may block the passage of isolated clusters, so that the mobility of the charge carriers decreases. We have shown in the previous section that the diffuse scattering from the isolated defect clusters increases with dopant concentration, and so, despite trapping some of the vacancies in large aggregates, the number of mobile defects is increasing with x. Thus it appears that the blocking mechanism is responsible for the observed reduction in the superionic conductivity in $(ZrO_2)_{1-x}(Y_2O_3)_x$ with increasing yttria content.

VI. CONCLUSIONS

The crystal structure of the anion-deficient fluorite $(ZrO_2)_{1-x}(Y_2O_3)_x$ is extremely complex, containing three distinct types of defect cluster and showing considerable variation as a function of dopant concentration and temperature. The detailed information concerning the lattice disorder provided by this work highlights the need to perform both x-ray and neutron diffraction investigations to probe the locations of both cation and anion species and illustrates the importance of coherent diffuse scattering studies to determine the defect geometries. Only by detailed (time-consuming) studies over wide composition and temperature ranges can the true nature of these defects be proposed and

tested against experimental data and the interaction between structure and ionic conductivity established. Nevertheless, the lattice defects show strong structural relationships to the phases observed at lower (T-ZrO_2) and higher ($Zr_3Y_4O_{12}$) concentrations of dopant Y^{3+}. This observation remains to be proved as a general rule for the structural description of anion-deficient (or, indeed, anion-excess) fluorites, but it does provide a pointer for the development of plausible de-

fect cluster models which can be tested against experimental data.

ACKNOWLEDGMENTS

[1] S. Chandra, *Superionic Solids: Principles and Applications* (North-Holland, Amsterdam, 1981).

[2] E. C. Subbarao, in *Science and Technology of Zirconia*, edited by A. H. Heuer (American Ceramic Society, Columbus, OH, 1981), p. 1.

[3] N. Q. Minh, J. Am. Ceram. Soc. **76**, 563 (1993).

[4] R. W. G. Wyckoff, *Crystal Structures* (Interscience, New York, 1963), Vol. 1.

[5] G. Teufer, Acta Crystallogr. **15**, 1187 (1962).

[6] B. H. O'Connor and T. M. Valentine, Acta Crystallogr., Sect. B: Struct. Crystallogr. Cryst. Chem. **25**, 2140 (1969).

[7] H. G. Scott, Acta Crystallogr., Sect. B: Struct. Crystallogr. Cryst. Chem. **33**, 281 (1977).

[8] H. G. Scott, J. Mater. Sci. **10**, 1527 (1975).

[9] V. S. Stubican, R. C. Hink, and S. P. Ray, J. Am. Ceram. Soc. **61**, 17 (1978).

[10] J. G. Allpress and H. J. Rossell, J. Solid State Chem. **15**, 68 (1975).

[11] B. Hudson and P. T. Mosely, J. Solid State Chem. **19**, 383 (1976).

[12] D. Steele and B. E. F. Fender, J. Phys. C **7**, 1 (1974).

[13] M. Morinaga, J. B. Cohen, and J. Faber, Jr., Acta Crystallogr., Sect. A: Cryst. Phys., Diffr., Theor. Gen. Crystallogr. **35**, 789 (1979).

[14] M. Morinaga, J. B. Cohen, and J. Faber, Jr., Acta Crystallogr., Sect. A: Cryst. Phys., Diffr., Theor. Gen. Crystallogr. **36**, 520 (1980).

[15] J. Faber, Jr., M. H. Müller, and B. R. Cooper, Phys. Rev. B **17**, 4884 (1978).

[16] H. Horiuchi, A. J. Schulz, P. C. W. Leung, and J. M. Williams, Acta Crystallogr., Sect. B: Struct. Sci. **40**, 367 (1984).

[17] C. J. Howard, R. J. Hill, and B. E. Reichert, Acta Crystallogr., Sect. B: Struct. Sci. **44**, 116 (1988).

[18] T. Proffen, M. Keilholz, R. B. Neder, F. Frey, and D. A. Keen, Acta Crystallogr., Sect. B: Struct. Sci. **52**, 66 (1996).

[19] R. B. Neder, F. Frey, and H. Schulz, Acta Crystallogr., Sect. A: Found. Crystallogr. **46**, 799 (1990).

[20] T. Proffen, R. B. Neder, and F. Frey, Acta Crystallogr., Sect. B: Struct. Sci. **52**, 59 (1996).

[21] T. Proffen, R. B. Neder, F. Frey, and W. Assmus, Acta Crystallogr., Sect. B: Struct. Sci. **49**, 599 (1993).

[22] T. Proffen, R. B. Neder, F. Frey, D. A. Keen, and C. M. E. Zeyen, Acta Crystallogr., Sect. B: Struct. Sci. **49**, 605 (1993).

[23] T. R. Welberry, R. L. Withers, J. G. Thompson, and B. D. Butler, J. Solid State Chem. **100**, 71 (1992).

[24] T. R. Welberry, B. D. Butler, J. G. Thompson, and R. L. Withers, J. Solid State Chem. **106**, 46 (1993).

[25] D. N. Argyriou, J. Appl. Crystallogr. **27**, 155 (1994).

[26] D. N. Argyriou and C. J. Howard, J. Appl. Crystallogr. **28**, 206 (1995).

[27] D. N. Argyriou, M. M. Elcombe, and A. C. Larson, J. Phys. Chem. Solids **57**, 183 (1996).

[28] I. R. Gibson and J. T. S. Irvine, J. Mater. Chem. **6**, 895 (1996).

[29] R. Osborn, N. H. Andersen, K. Clausen, M. A. Hackett, W. Hayes, M. T. Hutchings, and J. E. Macdonald, Mater. Sci. Forum **7**, 55 (1986).

[30] N. H. Andersen, K. Clausen, M. A. Hackett, W. Hayes, M. T. Hutchings, J. E. Macdonald, and R. Osborn, Physica B **136**, 315 (1986).

[31] S. Hull, T. W. D. Farley, M. A. Hackett, W. Hayes, R. Osborn, N. H. Andersen, K. Clausen, M. T. Hutchings, and W. G. Stirling, Solid State Ionics **28–30**, 488 (1988).

[32] H. Morikawa, Y. Shimizugawa, F. Marumo, T. Harasawa, H. Ikawa, K. Tohji, and Y. Udagawa, J. Jpn. Ceram. Soc., **96**, 253 (1988).

[33] Z. J. Shen, T. K. Li, K. Q. Lu, and Y. Q. Zhao, Guisuanyan Xuebao **16**, 270 (1988).

[34] M. H. Tuilier, J. Dexpert-Ghys, H. Dexpert, and P. Lagarde, J. Solid State Chem. **69**, 153 (1987).

[35] X. Li and B. Hafskjold, J. Phys.: Condens. Matter **7**, 1255 (1995).

[36] P. Li, I-W. Chen, and J. E. Penner-Hahn, Phys. Rev. B **48**, 10 074 (1993).

[37] C. R. A. Catlow, A. V. Chadwick, G. N. Greaves, and L. M. Moroney, J. Am. Ceram. Soc. **69**, 272 (1986).

[38] M. Cole, C. R. A. Catlow, and J. P. Dragun, J. Phys. Chem. Solids **51**, 507 (1990).

[39] F. Shimojo, T. Okabe, F. Tachibana, M. Kobayashi, and H. Okazaki, J. Phys. Soc. Jpn. **61**, 2848 (1992).

[40] C. H. Perry and A. Feinberg, Solid State Commun. **36**, 519 (1980).

[41] C. León, M. L. Lucía, and J. Santamaría, Phys. Rev. B **55**, 882 (1997).

[42] J. D. Solier, I. Cachadiña, and A. Dominguez-Rodriguez, Phys. Rev. B **48**, 3704 (1993).

[43] E. C. Subbarao and T. V. Ramakrishnan, in *Fast-Ion Transport in Solids*, edited by P. Vashista, J. N. Mundy, and G. K. Shenoy (Elsevier, New York, 1979), p. 653.

[44] D. K. Hohnke, in *Fast-Ion Transport in Solids*, edited by P. Vashista, J. N. Mundy, and G. K. Shenoy (Elsevier, New York, 1979), p. 449.

[45] H. W. Brinkman, W. J. Briels, and H. Verweij, Chem. Phys. Lett. **247**, 386 (1995).

[46] A. Nakamura and J. B. Wagner, Jr., J. Electrochem. Soc. **133**, 1542 (1986).

[47] C. R. A. Catlow, Solid State Ionics **12**, 67 (1984).

[48] H. Schmalzried, Z. Phys. Chem. (Neue Folge) **105**, 47 (1977).

[49] D. Y. Wang, D. S. Park, J. Griffith, and A. S. Nowick, Solid State Ionics **2**, 95 (1981).

[50] A. Nakamura and J. B. Wagner, Jr., J. Electrochem. Soc. **127**, 2325 (1980).

[51] M. Meyer and N. Nicoloso, Ber. Bunsenges. Phys. Chem. **101**, 1393 (1997).

[52] M. Meyer, N. Nicoloso, and V. Jaenisch, Phys. Rev. B **56**, 5961 (1997).

[53] L. Van Hove, Phys. Rev. **95**, 249 (1954).

[54] D. A. Keen, M. J. Harris, and W. I. F. David, Physica B **241-243**, 201 (1998).

[55] W. C. Hamilton, Acta Crystallogr. **18**, 502 (1965).

[56] K. J. McClellan, S. Q. Xiao, K. P. D. Lagerlof, and A. H. Heuer, Philos. Mag. A **70**, 185 (1994).

[57] M. R. Thornber and D. J. M. Bevan, J. Solid State Chem. **1**, 536 (1970).

[58] S. P. Ray, V. S. Stubican, and D. E. Cox, Mater. Res. Bull. **15**, 1419 (1980).

[59] R. B. von Dreele, L. Eyring, A. L. Bowman, and J. L. Yarnell, Acta Crystallogr., Sect. B: Struct. Crystallogr. Cryst. Chem. **31**, 971 (1975).

[60] M. R. Thornber, D. J. M. Bevan, and J. Graham, Acta Crystallogr., Sect. B: Struct. Crystallogr. Cryst. Chem. **24**, 1183 (1968).

[61] H. J. Rossell, J. Solid State Chem. **19**, 103 (1976).

[62] H. J. Rossell and H. G. Scott, J. Solid State Chem. **13**, 345 (1975).

[63] J. G. Allpress, H. J. Rossell, and H. G. Scott, J. Solid State Chem. **14**, 264 (1975).

[64] H. Marxreiter, H. Boysen, F. Frey, H. Schulz, and T. Vogt, Mater. Res. Bull. **25**, 435 (1990).

[65] R. D. Shannon and C. T. Prewitt, Acta Crystallogr., Sect. B: Struct. Crystallogr. Cryst. Chem. **25**, 925 (1969).

[66] S. Hull and C. C. Wilson, J. Solid State Chem. **100**, 101 (1992).